

# SparseGS: Real-Time 360° Sparse View Synthesis using Gaussian Splatting

Haolin Xiong<sup>1\*</sup>, Sairisheek Muttukuru<sup>1\*</sup>, Rishi Upadhyay<sup>1</sup>, Pradyumna Chari<sup>1</sup>, and Achuta Kadambi<sup>1</sup>

University of California, Los Angeles  
{xiongh,sairisheekm,rishiu,pradyumnac}@ucla.edu  
achuta@ee.ucla.edu

**Abstract.** The problem of novel view synthesis has grown significantly in popularity recently with the introduction of Neural Radiance Fields (NeRFs) and other implicit scene representation methods. A recent advance, 3D Gaussian Splatting (3DGS), leverages an explicit representation to achieve real-time rendering with high-quality results. However, 3DGS still requires an abundance of training views to generate a coherent scene representation. In few shot settings, similar to NeRF, 3DGS tends to overfit to training views, causing background collapse and excessive floaters, especially as the number of training views are reduced. We propose a method to enable training coherent 3DGS-based radiance fields of 360° scenes from sparse training views. We integrate depth priors with generative and explicit constraints to reduce background collapse, remove floaters, and enhance consistency from unseen viewpoints. Experiments show that our method outperforms base 3DGS by 6.4% in LPIPS and by 12.2% in PSNR, and NeRF-based methods by at least 17.6% in LPIPS on the MipNeRF-360 dataset with substantially less training and inference cost.

## 1 Introduction

The problem of learning 3D representations from 2D images has long been of interest, but has always been a difficult challenge due to the inherent ambiguities in lifting data to higher dimensions. Neural Radiance Fields (NeRFs) [1, 2, 18] tackle this problem by training a neural network using 2D posed images to predict the color and density of points in 3D space. The simplicity and quality of NeRFs enabled significant advances in novel view synthesis and led to a flurry of follow-up work. 3D Gaussian Splatting [11], a more recent technique, builds off of the ideas of NeRFs but replaces the implicit neural network with with an explicit representation based on 3D gaussians. These gaussians are rendered using point-based splatting, which allows for high rendering speeds, but requires fine-grained hyperparameter tuning. While NeRFs and 3D gaussian splatting both perform well at the task of novel view synthesis, they tend to require large

---

\* These authors contributed equally to this work

sets of training views, which can be difficult due to reasons such as variable lighting conditions, weather-dependent constraints, and logistical complexities. As a result, interest in techniques for few-shot novel view synthesis has grown.

The few-shot view synthesis problem is especially difficult because the inherent ambiguity in learning 3D structure from 2D images is significantly exacerbated: with few-views, many regions of scene have little to no coverage. Therefore, there are many possible incorrect 3D representations that can represent the 2D training views correctly but will have poor results when rendering novel views due to artifacts such as "floaters" [2], floating regions of high density irregularly positioned through the scene, "background collapse", when the background is represented by similar looking artifacts closer to cameras, or holes in the representation. Previous works have tackled this problem through the introduction of constraints that regularize the variation between views or the rendered depth maps. To our knowledge, most recent prior works in this area are built on top of NeRF and as a result are limited by long training times and the inherent black-box nature of neural networks. The lack of transparency poses a notable constraint, preventing a direct approach to the problem at hand. Instead, these challenges are approached indirectly through the use of meticulously designed loss functions and constraints.

In this work, we introduce a technique for few-shot novel view synthesis built on top of 3D Gaussian Splatting. The explicit nature of our underlying representations enables us to introduce a key new operation: direct floater pruning. This operation identifies the parts of a rendered image that suffer due to floaters or background collapse and allows us to **directly edit** the 3D representation to remove these artifacts. As a result, we are afforded greater control over when this operation is applied and how selective it is based on the scene representation during training. We show that this operation provides significant benefits in common view synthesis metrics and allows us to operate on full 360° unbounded scenes, a setting which most current few-shot techniques do not handle. In addition to this new operator, we leverage recent advances in image generation diffusion models to provide supervision in regions with little coverage from training views and apply depth constraints based on a novel technique for rendering depth from 3D gaussians which allows for better depth optimization. Together, we show that these techniques can enable high-quality novel-view synthesis from sparse views that out-performs prior state of the art work.

### 1.1 Contributions

In summary, we make the following contributions:

1. We propose a novel technique for training 3D radiance fields from few-views in unbounded 360° settings. We show that our technique provides improvements of up to 6.4% over Base 3DGS in and at least 17.6% over NeRF-based methods in LPIPS.
2. We develop a novel technique to estimate depth from a 3D Gaussian representation that allows for better depth optimization.
3. We introduce a new explicit, adaptive operator on 3D representations to prune unwanted "floater" artifacts in point-based 3D representations.

## 2 Related Work

**Radiance Fields** Radiance Fields, 3D representations of radiance in a scene, were first introduced by Neural Radiance Fields [18] (NeRFs) which represent 3D scenes with a neural volumetric representation that learns a density and color for every point. If density is represented by  $\sigma$  and color as  $c$ , the final color of a ray can be written using volumetric rendering principles as a combination of the density and color at the sample points along the ray as follows:

$$C = \sum_i T_i \sigma_i c_i \quad (1)$$

where  $T_i$  is the transmittance representing the probability of getting to sample point without intersecting a particle before. NeRFs are then trained using gradient descent on an image reconstruction loss. NeRFs have encouraged a flurry of follow-up work for extending NeRFs with new types of data [12, 17], improving speed [20] or quality [1], or applying them to novel tasks [38, 43]. A set of NeRF follow-ups that are particularly relevant to our topic are Mip-NeRF [1] and Mip-NeRF 360 [2]. Mip-NeRF [1] introduced the concept of anti-aliasing to NeRFs by rendering conical frustums rather than just single rays. As a result, they are able to anti-alias their renders and render at multiple resolutions at high quality. Mip-NeRF 360 was a follow-up work to Mip-NeRF that specifically tackled the problem of representing 360° unbounded scenes. We also focus on this setting in this work as it is a challenging setting for sparse view techniques.

While NeRFs rely on a neural network to represent the radiance field, 3D Gaussian Splatting [11], is a recent technique for view synthesis that replaces the neural network with explicit 3D Gaussians. These gaussians are parameterized by their position, rotation, scaling, opacity, and a set of spherical harmonics coefficients for view-dependent color. They are then rendered by projecting the gaussians down to the image plane using splatting-based rendering techniques [47, 48] and then alpha blending the resulting colors and opacities. Models trained using the same reconstruction loss as NeRFs. Replacing ray-tracing and neural network process of NeRF-based methods with splatting and direct representation process offers significant run-time improvements and allows for real-time rendering during inference. In addition, 3D Gaussian representations are explicit rather than the implicit representations of NeRFs, which allows for more direct editing and easier interpretability. We leverage this property for our technique which identifies and directly deletes floaters. Recent works have built on top of 3D gaussian splatting to perform a variety of downstream tasks including text-to-3d generation [34, 42], dynamic scene representation [15, 39], and animating humans [46]. However, to our knowledge, we are one of the first to provide a technique for few-shot novel view synthesis using 3D gaussians.

**Few Shot Novel View Synthesis** The problem of novel view synthesis from few images has received significant interest as many view synthesis techniques can require a prohibitively high number of views for real-world usage. Many early

techniques [30, 35, 44] leverage multi-plane images (MPIs), which represent images by sub-images at different depths, to re-render depth and color from novel view points using traditional transformations. More recent techniques are built on top of the NeRF framework and tend to tackle the problem one of two ways: The first set of methods introduce constraints on the variation between views. An early example of this type of method was DietNeRF [9] which added constraints to ensure that high-level semantic features remained the same from different views since they contained the same object. Another example is RegNeRF [21] which applies both color and depth consistency losses to the outputs at novel views. ViP-NeRF [29] modifies the traditional NeRF framework to additionally compute the visibility of a point and then uses these outputs to regularize the visibility and alpha-blended depth of different views. The second set of methods approach the problem by adding depth priors to novel views to regularize outputs. SparseNeRF [36] falls into this category and uses a pre-trained depth estimation model to get pseudo-ground truth depth maps which are then used for a local depth ranking loss. They additionally apply a depth smoothness loss to encourage rendered depth maps to be piecewise-smooth. DSNeRF [3] also uses additional depth supervision, but uses the outputs of the SfM pipeline (typically COLMAP [27, 28]) used to get camera poses instead of a pre-trained model. Beyond these two techniques, some prior works approach the problem through recent machine learning techniques. Specifically, Neo 360 [7] uses a tri-plane feature representation to enable their model to reason about 3D features more robustly. A recent technique, FSGS [45], also utilizes 3D Gaussians for sparse-view synthesis. This approach introduces an unpooling operation to densify Gaussians in a novel manner and also incorporates depth priors for enhanced performance. However, FSGS is designed to use 24 views, while all of our results use 12 or fewer. To our knowledge, Neo360 and FSGS are the only other techniques that explicitly tackle the problem of 360°-few-shot novel-view synthesis.

### 3 Methods

Our method is comprised of four key components: a depth correlation loss, a diffusion loss, an image re-projection loss, and a floater pruning operation.

#### 3.1 Rendering Depth from 3D Gaussians

Many of the components we introduce rely on depth maps rendered from the 3D Gaussian representation. In order to compute these, we utilize three different techniques, each with different properties: alpha-blending, mode-selection, and softmax scaling. To our knowledge, mode-selection and softmax scaling are novel depth rendering techniques.

**Alpha-blending** Alpha-blending renders depth maps by following the same procedure used for rendering color images. Let  $d_{x,y}^{\text{alpha}}$  denote the alpha-blended

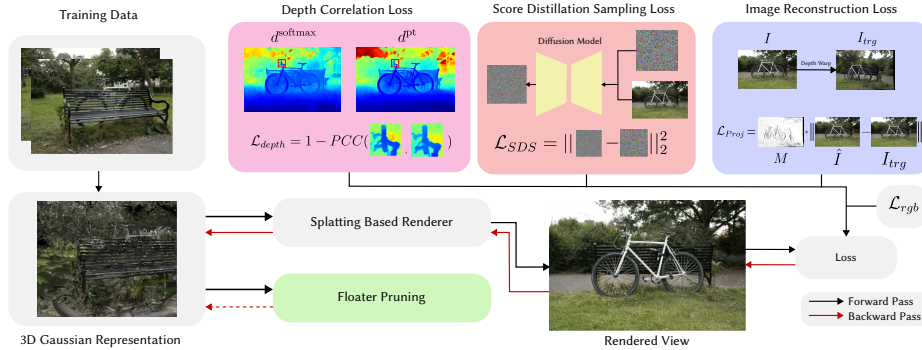


**Fig. 1: Our proposed pipeline incorporates depth priors, diffusion constraints, and a floater pruning technique to improve few-shot novel view synthesis performance.** During training, we render the softmax depth and use Pearson correlation to encourage it to align with  $d^{pt}$  as described in Sec. 3.2. We also generate novel views using the procedure described in Sec. 3.3 and incorporate a score distillation sampling loss. At pre-set intervals, we prune floaters as described in Sec. 3.5. New components we propose are colored while the base 3DGS pipeline is in grey.

depth at a pixel  $x, y$ , we can calculate it as:

$$d_{x,y}^{alpha} = \sum_{i=1}^N T_i \alpha_i d_i \tag{2}$$

where  $T_i$  is the accumulated transmittance for the  $i$ th gaussian,  $\alpha_i$  is the alpha-compositing weight, and  $d_i$  is the depth of the gaussian. (In our model, the sum  $\sum_{i=1}^N T_i \alpha_i$  is almost always 1.)

**Mode-selection** In mode-selection, the depth of the gaussian with the largest contributing  $w_i = T_i \alpha_i$  represents the depth of that pixel. The mode-selected depth of a pixel can be written as:

$$d_{x,y}^{mode} = d_{\arg \max_i (w_i)} \tag{3}$$

Intuitively, the mode-selected depth can be thought of as choosing the first high opacity gaussian while the alpha blended depth considers almost all gaussians along an imaginary ray from the camera. A key insight that we will rely on later to build our pruning operator is that  $d^{mode}$  and  $d^{alpha}$  are not always the same even though they should be in the ideal case. Consider the toy setting on the left of Fig. 2.  $d^{mode}$  is the depth of the second gaussian from the left since that is the one with the highest  $w_i$ , but  $d^{alpha}$  appears slightly behind this gaussian due to low weight gaussians with higher depths. This difference can lead to ambiguity about what the true depth is. We interpret this ambiguity as a measure of the uncertainty of 3DGS at a point and use it to inform our pruning operator introduced later.

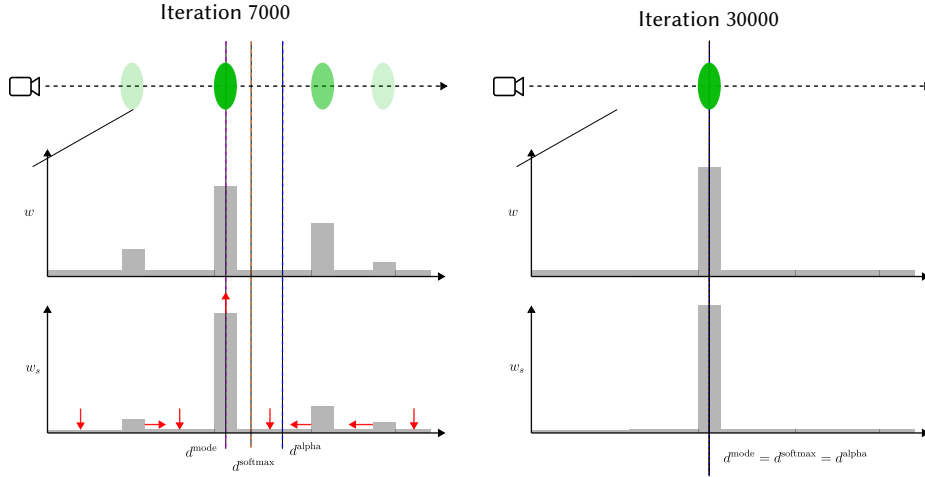


**Fig. 2: A toy example that demonstrates the different kinds of depth: mode, alpha-blended, and softmax, we use in our technique and how our depth correlation loss affects gaussian weights  $w_i$ .**  $w_i$  are shown on top and the weights after applying softmax are below. **Left:** Gaussian and weight distribution after 7000 iterations of training. Although there is a single gaussian with the highest weight, there are other low-weight gaussians nearby that affect both the rendering quality and the calculated depths. Shown in red, our loss encourages these smaller peaks to come closer to the tallest peak while also encouraging empty regions to go close to 0. **Right:** After training is complete, our depth correlation loss has consolidated low-weight gaussians into a single gaussian at the correct depth. All of our depth variations now agree.

**Softmax-scaling** Although the mode depth works quite well for this purpose of identifying ambiguity in depth, the presence of the arg max operator in its equation means that any backward gradients only flow to one gaussian, the one with the highest  $w_i$ . This is not ideal, as we would like to influence all gaussians along this imaginary ray to converge on the correct depth. In order to overcome this limitation of the mode depth, we introduce a new method to render depth that is a mix of the both alpha-blending and mode-selection, called the softmax depth:

$$d_{x,y}^{\text{softmax}} = \log \left( \frac{\sum_{i=1}^N w_i e^{\beta w_i} d_i}{\sum_{i=1}^N w_i e^{\beta w_i}} \right) \quad (4)$$

where the  $\beta$  parameter allows us to modulate the softmax temperature, thereby choosing a desired amplification of highly weighted gaussians. Note that:

$$\lim_{\beta \rightarrow 0} d_{x,y}^{\text{softmax}} = \log(d_{x,y}^{\text{alpha}}) \quad (5)$$

$$\lim_{\beta \rightarrow \infty} d_{x,y}^{\text{softmax}} = \log(d_{x,y}^{\text{mode}}) \quad (6)$$

Compared to mode depth, with the softmax approach, we can approximate the mode depth while still propagating gradients to gaussians surrounding the mode. We additionally compute a pseudo-ground truth depth map using a pre-trained depth estimation model on top of the training views. We use Monodepth [16, 31] but any pre-trained depth estimation model [24, 25] can work. We refer to the depth from this pre-trained model as  $d^{pt}$ .

### 3.2 Patch-based Depth Correlation Loss

Since the monocular estimation model predicts relative depth while our alpha-blended and mode-based depths are COLMAP-anchored depth, directly applying a loss such as mean squared error (MSE) would not work well. One option is to attempt to estimate scale and shift parameters and use those to align the two depth maps in metric space. However, the transformation between the depth maps is not guaranteed to be constant at all points, meaning a naive alignment could introduce additional unwanted distortion. Instead, we propose utilizing Pearson correlation across image-patches to compute a similarly metric between depth maps. This is similar to the depth ranking losses proposed by prior work [36], but instead of comparing two selected points per iteration, we compare entire patches, meaning we can affect larger portions of the image at once and can learn more local structure. The Pearson correlation coefficient is closely related to normalized cross-correlation; therefore, employing this loss encourages patches at the same location in both depth maps to have high cross-correlation, irrespective of the variations in depth value ranges.

At each iteration, we randomly sample  $N$  non-overlapping patches to compute the depth correlation loss as:

$$\mathcal{L}_{depth} = \frac{1}{N} \sum_i^N 1 - PCC(p_i^{softmax}, p_i^{pt}) \quad (7)$$

$$PCC(X, Y) = \frac{\mathbb{E}[XY] - \mathbb{E}[X]\mathbb{E}[Y]}{\sqrt{\mathbb{E}[Y^2] - \mathbb{E}[Y]^2} \sqrt{\mathbb{E}[X^2] - \mathbb{E}[X]^2}} \quad (8)$$

where  $p_i^{softmax} \in \mathbb{R}^{S^2}$  denotes the  $i$ th patch of  $d^{softmax}$  and  $p_i^{pt} \in \mathbb{R}^{S^2}$  denotes the  $i$ th patch of  $d^{pt}$ , with the patch size  $S$  being a hyper-parameters. Intuitively, this loss works to align the softmax depth maps of the gaussian representation with the depth map of monodepth while avoiding the problem of inconsistent scale and shift.

### 3.3 Score Distillation Sampling Loss

In the few-shot setting, the sparsity of the input training data likely results in incomplete coverage of the scene. Therefore, inspired by recent advancements in image generative models [5, 8, 22, 26, 34, 41], we propose using a pre-trained generative diffusion model to refine the 3D gaussian representation via Score Distillation Sampling (SDS) as introduced in [23]. This allows us to refine plausible

details for regions that do not have perfect coverage in the training views and generate more complete 3D representations [6, 13, 14, 32]. Our implementation starts by generating novel camera poses within the camera-to-world coordinate system. We simply sample random views aimed at the scene center from an elliptic cylinder best fit to the training view positions. The SDS loss can then be formulated as:

$$\hat{I} = \mathcal{N}(\sqrt{\hat{\alpha}}I', (1 - \hat{\alpha})\mathbf{I}) \quad (9)$$

$$\mathcal{L}_{SDS} = \nabla_G \mathbb{E}[(\epsilon_\phi(\hat{I}_p; \tilde{I}_p) - \epsilon) \frac{\partial \hat{I}_p}{\partial G}] \quad (10)$$

where  $G$  represents the parameters of our gaussian representation,  $\hat{\alpha}$  represents the cumulative product of one minus the variance schedule and  $\epsilon$  is the noise introduced by the SDS,  $\epsilon_\phi(\cdot)$  is the predicted noise by Stable Diffusion,  $\hat{I}_p$  is the rendered image at camera pose  $p$  with added noise, and  $\tilde{I}_p$  is the image denoised by Stable Diffusion. Intuitively, the SDS loss first finds the error between the true noise added to an image and the error the diffusion model estimates and then takes the gradient of this error with respect to the parameters of our gaussian model, i.e. the means, scalings, rotations, and opacities of the gaussians. Note that our usage of this SDS loss differs greatly from most prior uses of diffusion models for sparse view synthesis. While most prior techniques leverage diffusion models in order to fill-in large blank regions or hallucinate new views that are not present in the original images (e.g. if we only have a front view and use diffusion to hallucinate a back view), we use diffusion models and the SDS loss only as a refinement step to improve our renders which are expected to already include most of the correct structure of our 3D scene.

### 3.4 Image Re-projection Loss

Most 3D reconstruction models operate by fitting to the training views in the hope that the model can learn the underlying geometry of the scene. However, this approach becomes problematic in settings with extremely sparse input, as the model tends to overfit excessively [9, 21]. This overfitting leads to background collapse even with minimal changes in the viewing angle, undermining the model’s ability to generalize and accurately reconstruct the scene from new perspectives. In our study, we employ image re-projection, which utilizes established depth warping techniques [3, 19, 40] to augment the available training data by re-projecting images to novel viewpoints.

It is impractical to perform depth warping directly using outputs from the Monodepth model because they are in a relative scale between 0 and 1. However, we have discovered a solution to this limitation by scaling the range of 0 to 1 to match the minimum and maximum values of rendered alpha-blended depth maps. As a result, the quality of the warping is highly dependent on the estimation of  $\min_i d_i^{alpha}$  and  $\max_i d_i^{alpha}$ ; however, in practical applications, we have observed that the warping results are quite stable, provided that the depth Pearson loss has converged to a reasonable level. This finding underscores the

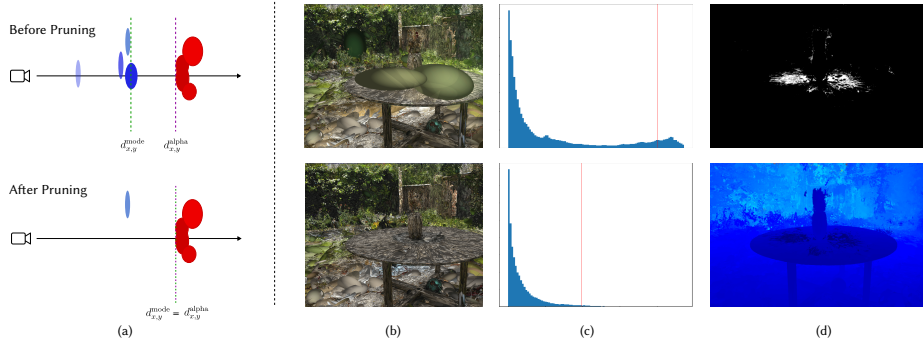


**Fig. 3: The proposed floater pruning technique removes gaussians at inaccurate depths.** A toy example (a) demonstrates the pruning technique: before pruning, there are floaters (blue) in front of the gaussians at the object surface (red) and therefore,  $d_{x,y}^{mode} \neq d_{x,y}^{alpha}$ . The pruning technique removes all gaussians on that pixel before the mode and as a result,  $d_{x,y}^{mode} = d_{x,y}^{alpha}$ . Applied to the garden scene (b), the pruning technique removes large floaters in the center and left of the scene. We see the link between the bimodality of the histogram of relative differences before and after the pruning operator in (c), with the appropriate pruning cutoff points indicated by the red vertical line. (d) top: The floater mask  $F_i$  is obtained from thresholding the relative differencing of the mode depth  $d^{mode}$  (bottom) at the cutoff points.

potential of leveraging scaled monodepth outputs for effective depth warping in a variety of contexts.

Mathematically, we can define our image re-projection as follows: For pixel  $p_i(x_i, y_i)$  in training image  $I_{src}$ , the warping to the corresponding pixel  $p_j(x_j, y_j)$  at an unseen viewpoint  $I_{trg}$  can be formulated as:

$$p_j = K_{trg} T(K_{src}^{-1} Z_i p_i) \tag{11}$$

where  $Z_i$  is the monodepth outputs scaled to the range of  $\min_i d_i^{alpha}$  and  $\max_i d_i^{alpha}$ ,  $K_{trg}$  and  $K_{src}$  are the intrinsic matrices of the source and the target camera, and  $T$  refers to the transformation between camera poses from viewpoint  $I_{src}$  to  $I_{trg}$ . A warp mask  $M$ , which marks which pixels were validly warped, is generated along with the process. The image re-projection loss  $L_{Proj}$  is formulated as:

$$\mathcal{L}_{Proj} = M * L_1(\hat{I}, I_{trg}) \tag{12}$$

### 3.5 Floater Removal

Although the model is trained with the depth correlation loss, optimizing the softmax depth alone does not solve the problem of "floaters". An example image with floaters is shown in Fig. 3b. In order to remove floaters, we propose a novel operator which leverages the explicit representation of 3D gaussians to remove floaters and encourages the model to re-learn those regions of the training views

**ALGORITHM 1:** Algorithm to prune floaters

---

```

Function prune_floaters( $G, P, a, b$ )
  Input : Gaussian Representation  $G$ 
  Input : Camera Poses  $P$ 
  Input : Curve Parameters  $a, b$ 
   $\bar{D} \leftarrow 0.0$ 
  foreach  $p \in P$  do
     $d^{\text{alpha}} \leftarrow \text{alpha\_blend\_depth}(G, p)$ 
     $d^{\text{mode}} \leftarrow \text{mode\_select}(G, p)$ 
     $\Delta_p \leftarrow \frac{d^{\text{mode}} - d^{\text{alpha}}}{d^{\text{alpha}}}$ 
     $\bar{D} \leftarrow \bar{D} + \text{dip\_test}(\Delta_p)$ 
  end
   $\bar{D} \leftarrow \bar{D} / |P|$ 
  foreach  $p \in P$  do
     $\tau_p \leftarrow \text{percentile}(\Delta_p, ae^{b\bar{D}})$ 
     $F_p \leftarrow \mathbb{1}[\Delta_p > \tau]$ 
     $g_0, g_1, \dots, g_n \leftarrow \text{mask\_to\_gaussian}(F_p)$ 
    remove\_gaussians( $g_0, g_1, \dots, g_n$ )
  end
end

```

---

correctly. In our model, "Floaters" often manifest themselves as relatively low opacity gaussians positioned close to the camera plane. As a result, although they do not appear prominently when we render the softmax depth of a scene because they are "averaged out", they are prominent in the mode-selected depth. We leverage this difference to generate a floater mask  $F$  for each training view. Having identified this mask in image space, we then select and prune all gaussians up-to and including the mode gaussian. Specifically, we compute  $F$  for a single training view  $i$  as follows: we first compute  $\Delta_i$ , the relative difference between the mode-selected depth and alpha-blended depth. When visualizing the distributions of  $\Delta_i$ , we noticed that images with many floaters had bi-modal histograms, as floaters tend to be far from the true depth, while images without floaters tended to be more uni-modal. We visualize this phenomenon in Fig. 3. Leveraging this, we perform the dip test [4], a measure of uni-modality, on the distribution. We then average the uni-modality score across all training views for a scene, since the number of floaters is generally a scene wide metric, and use the mean to select a cut-off threshold for the relative differences. The dip statistic to threshold conversion process is performed using an exponential curve with parameters  $a, b$ . We estimate these parameters by manually examining  $\Delta_i$  and  $F_i$  for various scenes from different datasets and real world capture. This process was carefully designed to allow our floater pruning to be adaptive: in some cases, our 3D scenes are already quite high quality and as a result do not have many floaters. In that situation, if we set a pre-defined threshold for the percent of pixels to prune, we would be forcing ourselves to delete detail from

| Model        | PSNR ↑         | SSIM ↑        | LPIPS ↓       | Time (h) |
|--------------|----------------|---------------|---------------|----------|
| SparseNeRF   | 11.5638        | 0.3206        | 0.6984        | 4        |
| RegNeRF      | 11.7379        | 0.2266        | 0.6892        | 4        |
| Mip-NeRF 360 | <u>17.1044</u> | <u>0.4660</u> | 0.5750        | 3        |
| Base 3DGS    | 15.3840        | 0.4415        | <u>0.5061</u> | 0.5      |
| Ours         | <b>17.2558</b> | <b>0.5067</b> | <b>0.4738</b> | 0.75     |

(a)

| Model     | PSNR ↑         | SSIM ↑        | LPIPS ↓       | Time (h) |
|-----------|----------------|---------------|---------------|----------|
| DSNeRF    | <b>17.4934</b> | 0.3620        | 0.6242        | 4        |
| Base 3DGS | 15.2437        | <u>0.3914</u> | <u>0.4824</u> | 0.5      |
| Ours      | <u>16.7740</u> | <b>0.4341</b> | <b>0.4390</b> | 0.75     |

(b)

**Table 1: Our model out-performs previous SOTA on SSIM and LPIPS for few-shot novel view synthesis on the Mip-NeRF 360 dataset.** Results in (a) were rendered at 1/2x while Results in (b) were at 1/4x resolution due to memory constraints with DSNeRF. All models in the same table were run at the same resolution for fairness. Training times were recorded on 1 RTX3090

the scene. Similarly, some scenes are especially difficult to learn (due to the 3D structure or distribution of training images) and in those cases, we would like our pruning to remove more floaters than normal. The average dip score  $\bar{D}$  provides a proxy measure of how many floaters a scene contains and allows us to adjust our techniques in response. Our full pruning process is visualized in Fig. 3 and shown in Algorithm 1.

**Full Loss** Combined, our full loss is:

$$\mathcal{L} = \mathcal{L}_{rgb}(\hat{I}, I) + \lambda_{depth} \mathcal{L}_{depth}(d^{\text{softmax}}, d^{\text{pt}}) + \lambda_{SDS} \mathcal{L}_{SDS}(\hat{I}') + \lambda_{Proj} \mathcal{L}_{Proj}(\hat{I}_{trg}, I_{trg}) \quad (13)$$

where  $\hat{I}$  is the rendered image,  $I$  is the ground truth image, and  $\hat{I}'$  is a rendered image from a random novel viewpoint (not a training view).  $\mathcal{L}_{rgb}$  is the same loss as is used to train base 3D Gaussian Splatting.

## 4 Results

### 4.1 Mip-NeRF 360 Dataset

Since our technique is focused on unbounded, 360° scenes, we evaluate on the Mip-NeRF 360 dataset designed specifically for this use case. The full dataset contains 9 scenes, but we select 6 of them which truly have 360° coverage. We compare against Mip-NeRF 360 [2], DSNeRF [3], SparseNeRF [36], RegNeRF [21], and base 3D Gaussian Splatting [11]. DSNeRF, RegNeRF, and SparseNeRF are specifically designed for the few-shot setting, but are focused on frontal scenes. Mip-NeRF 360 and 3D Gaussian Splatting are designed for the general view synthesis case, but are also designed to handle 360° scenes. Thus, we use them as comparison benchmarks in our evaluation. For this setting, we use 12 training views. Results on PSNR, SSIM, and LPIPS are shown in Tab. 1. We additionally compare the runtimes of all methods. We opted to split the evaluation into two tables due to limitations in memory: running DSNeRF at higher resolutions was not possible within these constraints. On the higher resolution comparison (against Mip-NeRF 360, SparseNeRF, etc.), we outperform

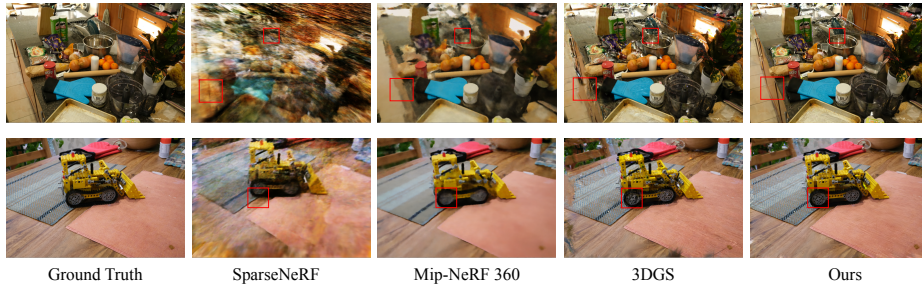


**Fig. 4: Qualitative results from the Mip-NeRF 360 dataset show our model produces images that are sharper and perceptually similar to ground truth.** Red boxes show specific regions of interest. Our model is able to reconstruct high-frequency detail such as the tires of the lego bulldozer and the plates while also maintaining coherence across the full image.

all baselines on SSIM, LPIPS and PSNR. Notably, we outperform Base 3DGS by 12.2% in PSNR and 14.8% in SSIM. For LPIPS specifically, we are 17.6% lower than the next best performing technique, Mip NeRF 360. We see a similar pattern for our comparison against DSNeRF where we outperform DSNeRF by 29.7% in LPIPS. Additionally, our technique trains in less than an hour and can run inference in real-time (100+ FPS). However, we are slightly outperformed by DSNeRF on PSNR. We believe this to be a result of the specific failure modes of our technique: NeRF based methods tend to face the problem of having outputs that are too smooth, which was what originally prompted the introduction of the positional encoding [18, 33]. As a result, in these few-shot settings, the renders from NeRF exhibit an overly smooth appearance. Conversely, the 3D gaussian representation gravitates towards positioning isolated gaussians in regions of empty space. As a result, when our model does not have a good representation of a scene region, we end up with high-frequency artifacts. PSNR tends to tolerate overly smooth outputs while heavily penalizing high-frequency artifacts [37], leading to the poor performance of our model when compared to NeRF baselines. On a perceptual metric such as LPIPS, we significantly outperform the next closest baseline.

## 4.2 DTU Dataset

In addition to Mip-NeRF 360, we provide comparisons on forward-facing scenes from the DTU dataset [10]. Although our technique is designed for unbounded 360° scenes, we provide these comparisons because a large set of prior work on the task of few-shot novel view synthesis has been focused on the forward-facing setting. Results can be seen in Tab. 2. Our model consistently outperforms Base 3DGS and is competitive with RegNeRF and SparseNeRF despite the fact that our method is designed for a different problem setting.



**Fig. 5: Our model visually outperforms DSNeRF for few-shot view synthesis.** Renders from DSNeRF can often be overly smooth due to the inherent nature of neural networks. Our representation is high quality in the scene center where we have high coverage, but can lose quality in the edges of an image.

| Model      | PSNR $\uparrow$ | SSIM $\uparrow$ | LPIPS $\downarrow$ | Model               | PSNR $\uparrow$ | SSIM $\uparrow$ | LPIPS $\downarrow$ |
|------------|-----------------|-----------------|--------------------|---------------------|-----------------|-----------------|--------------------|
| RegNeRF    | 18.89           | 0.745           | 0.190              | Base 3DGS           | 15.05           | 0.497           | 0.518              |
| SparseNeRF | 19.55           | 0.769           | 0.201              | + Depth Correlation | 16.52           | 0.587           | 0.438              |
| DSNeRF     | 16.90           | 0.570           | 0.450              | + Diffusion Loss    | 16.79           | 0.585           | 0.452              |
| Base 3DGS  | 14.18           | 0.6284          | 0.301              | + Depth Warping     | 16.93           | 0.598           | 0.438              |
| Ours       | 18.89           | 0.702           | 0.229              | + Floater Pruning   | <b>17.18</b>    | <b>0.602</b>    | <b>0.437</b>       |

**Table 2: Results on forward-facing scenes from the DTU dataset.** Our method is competitive with SOTA despite being designed for a different problem setting (unbounded 360 scenes). All models are trained with 3 input images.

**Table 3: An ablation study on the bonsai scene shows our full model performs best.** Each component individually provides benefits that combine to enable the performance of our full model. The best result is bolded.

### 4.3 Ablation Studies

We additionally run ablation studies to examine the effects of each of the individual components we introduce. Specifically, we ablate the depth correlation loss, the score distillation sampling loss, the image re-projection loss, and floater pruning. Results are shown in Tab. 3 and in Fig. 6. As can be seen in Tab. 3, our full model performs best on all three metrics, and the depth correlation loss, based on our novel depth formulation, provides the most benefit among the three components of our technique (drop of approx. 1.5 PSNR when removing it). Fig. 6 highlights the benefits of the depth correlation loss, particularly for the depth maps. Without the depth correlation loss, there are many discontinuities and sharp features in the depth map, likely because the model is excessively overfitting to the limited training views.

### 4.4 Implementation Details

Our training procedure is built on top of the procedure introduced in 3D Gaussian Splatting [11]. We train for 30k iterations with learning rates for the gaussian representation components taken from [11]. We apply the depth correlation loss every iteration with a patch size of 128 pixels and select 50% of all patches per iteration. We apply the diffusion loss randomly for 20% of iterations during the

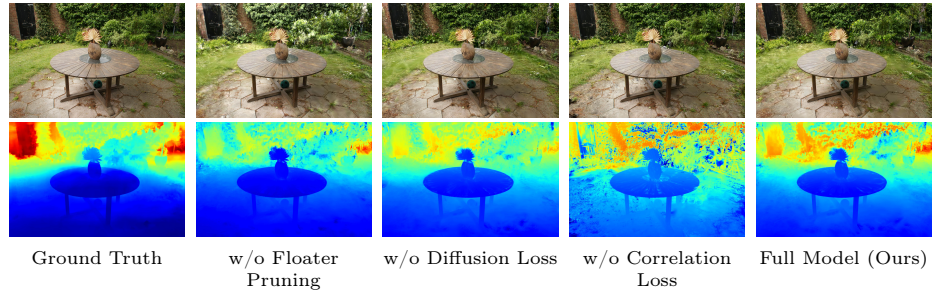


**Fig. 6: Our full model performs best in terms of image renders and depth maps.** Our full model combines the best of different subcomponents to generate high-quality depth maps (e.g. it retains the smoothness of the depth correlation loss while learning background details from floater pruning and diffusion). For depth maps, the ground truth is the output of the Monodepth model.



**Fig. 7: NeRF and 3DGS and suffer from different failure modes.** NeRF tends to oversmooth ambiguous areas of the scene, while 3DGS spawns many gaussians leading to high frequency artifacts. Additionally, NeRF based implicit methods can be queried anywhere in the 3D space, while explicit methods can only reconstruct areas covered in the training views. This leads to areas not covered by the training views to appear black while NeRF based methods exhibit a repeat padding appearance

last 10k steps. We additionally apply our floater pruning technique at 20k iteration with  $a = 97$  and  $b = -8$ . We choose  $\lambda_{depth} = 0.1$  and  $\lambda_{SDS} = 5 \times 10^{-4}$ . At 5k iteration, the point where the depth correlation loss has reasonably converged, alpha-blending depth maps are rendered for image re-projection. For each training camera, we generate 4 extra warping viewpoints by rotating it around the scene’s center. The projection weight  $\lambda_{Proj}$  is set to 0.3. We will release our code in the future.

## 5 Conclusion

*Limitations* One key limitation of our method is that because it is built on top of 3D Gaussian Splatting, it is heavily reliant on the initial point cloud provided by COLMAP. If this point cloud is inaccurate or lacks detail, our model may struggle to compensate adequately, leading to under-reconstructions, especially in areas distant from the scene center. This limitation is especially prominent in the sparse view setting, as our initial training views lack substantial coverage. As a result, the input point clouds are relatively small, with many tested scenes being initialized with fewer than 20 points in total. To address this challenge,

future efforts could involve investigating point cloud densification techniques as data augmentations.

In this paper, we introduce a novel 3D gaussian splatting based technique for few-shot novel view synthesis. We leverage the explicit nature of the 3D gaussian representation to introduce a novel pruning operator designed to reduce and remove "floater" artifacts. Applied to the Mip-NeRF 360 dataset, we show our technique can achieve state-of-the-art performance on few shot novel view synthesis for 360° unbounded scenes.

## References

1. Barron, J.T., Mildenhall, B., Tancik, M., Hedman, P., Martin-Brualla, R., Srinivasan, P.P.: Mip-nerf: A multiscale representation for anti-aliasing neural radiance fields. *ICCV* (2021) [1](#), [3](#)
2. Barron, J.T., Mildenhall, B., Verbin, D., Srinivasan, P.P., Hedman, P.: Mip-nerf 360: Unbounded anti-aliased neural radiance fields. *CVPR* (2022) [1](#), [2](#), [3](#), [11](#)
3. Deng, K., Liu, A., Zhu, J.Y., Ramanan, D.: Depth-supervised NeRF: Fewer views and faster training for free. In: *Proceedings of the IEEE/CVF Conference on Computer Vision and Pattern Recognition (CVPR)* (June 2022) [4](#), [8](#), [11](#)
4. Hartigan, J.A., Hartigan, P.M.: The Dip Test of Unimodality. *The Annals of Statistics* **13**(1), 70 – 84 (1985). <https://doi.org/10.1214/aos/1176346577>, <https://doi.org/10.1214/aos/1176346577> [10](#)
5. Ho, J., Jain, A., Abbeel, P.: Denoising diffusion probabilistic models. *Advances in neural information processing systems* **33**, 6840–6851 (2020) [7](#)
6. Hong, Y., Zhang, K., Gu, J., Bi, S., Zhou, Y., Liu, D., Liu, F., Sunkavalli, K., Bui, T., Tan, H.: Lrm: Large reconstruction model for single image to 3d. *arXiv preprint arXiv:2311.04400* (2023) [8](#)
7. Irshad, M.Z., Zakharov, S., Liu, K., Guizilini, V., Kollar, T., Gaidon, A., Kira, Z., Ambrus, R.: Neo 360: Neural fields for sparse view synthesis of outdoor scenes. In: *Proceedings of the IEEE/CVF International Conference on Computer Vision*. pp. 9187–9198 (2023) [4](#)
8. Jain, A., Mildenhall, B., Barron, J.T., Abbeel, P., Poole, B.: Zero-shot text-guided object generation with dream fields (2022) [7](#)
9. Jain, A., Tancik, M., Abbeel, P.: Putting nerf on a diet: Semantically consistent few-shot view synthesis. In: *Proceedings of the IEEE/CVF International Conference on Computer Vision (ICCV)*. pp. 5885–5894 (October 2021) [4](#), [8](#)
10. Jensen, R., Dahl, A., Vogiatzis, G., Tola, E., Aanæs, H.: Large scale multi-view stereopsis evaluation. In: *2014 IEEE Conference on Computer Vision and Pattern Recognition*. pp. 406–413. *IEEE* (2014) [12](#)
11. Kerbl, B., Kopanas, G., Leimkühler, T., Drettakis, G.: 3d gaussian splatting for real-time radiance field rendering. *ACM Transactions on Graphics* **42**(4) (July 2023), <https://repo-sam.inria.fr/fungraph/3d-gaussian-splatting/> [1](#), [3](#), [11](#), [13](#), [18](#)
12. Levis, A., Srinivasan, P.P., Chael, A.A., Ng, R., Bouman, K.L.: Gravitationally lensed black hole emission tomography. In: *Proceedings of the IEEE/CVF Conference on Computer Vision and Pattern Recognition*. pp. 19841–19850 (2022) [3](#)
13. Liu, M., Xu, C., Jin, H., Chen, L., Xu, Z., Su, H., et al.: One-2-3-45: Any single image to 3d mesh in 45 seconds without per-shape optimization. *arXiv preprint arXiv:2306.16928* (2023) [8](#)

14. Liu, R., Wu, R., Hoorick, B.V., Tokmakov, P., Zakharov, S., Vondrick, C.: Zero-1-to-3: Zero-shot one image to 3d object (2023) [8](#)
15. Luiten, J., Kopanas, G., Leibe, B., Ramanan, D.: Dynamic 3d gaussians: Tracking by persistent dynamic view synthesis. arXiv preprint arXiv:2308.09713 (2023) [3](#)
16. Miangoleh, S.M.H., Dille, S., Mai, L., Paris, S., Aksoy, Y.: Boosting monocular depth estimation models to high-resolution via content-adaptive multi-resolution merging. In: Proc. CVPR (2021) [7](#)
17. Mildenhall, B., Hedman, P., Martin-Brualla, R., Srinivasan, P.P., Barron, J.T.: NeRF in the dark: High dynamic range view synthesis from noisy raw images. CVPR (2022) [3](#)
18. Mildenhall, B., Srinivasan, P.P., Tancik, M., Barron, J.T., Ramamoorthi, R., Ng, R.: Nerf: Representing scenes as neural radiance fields for view synthesis. In: ECCV (2020) [1](#), [3](#), [12](#)
19. Mori, Y., Fukushima, N., Fujii, T., Tanimoto, M.: View generation with 3d warping using depth information for ftv. In: 2008 3DTV Conference: The True Vision - Capture, Transmission and Display of 3D Video. pp. 229–232 (2008). <https://doi.org/10.1109/3DTV.2008.4547850> [8](#)
20. Müller, T., Evans, A., Schied, C., Keller, A.: Instant neural graphics primitives with a multiresolution hash encoding. ACM Trans. Graph. **41**(4), 102:1–102:15 (Jul 2022). <https://doi.org/10.1145/3528223.3530127>, <https://doi.org/10.1145/3528223.3530127> [3](#)
21. Niemeyer, M., Barron, J.T., Mildenhall, B., Sajjadi, M.S.M., Geiger, A., Radwan, N.: Regnerf: Regularizing neural radiance fields for view synthesis from sparse inputs. In: Proc. IEEE Conf. on Computer Vision and Pattern Recognition (CVPR) (2022) [4](#), [8](#), [11](#)
22. Po, R., Yifan, W., Golyanik, V., Aberman, K., Barron, J.T., Bermano, A.H., Chan, E.R., Dekel, T., Holynski, A., Kanazawa, A., et al.: State of the art on diffusion models for visual computing. arXiv preprint arXiv:2310.07204 (2023) [7](#)
23. Poole, B., Jain, A., Barron, J.T., Mildenhall, B.: Dreamfusion: Text-to-3d using 2d diffusion. arXiv preprint arXiv:2209.14988 (2022) [7](#)
24. Ranftl, R., Bochkovskiy, A., Koltun, V.: Vision transformers for dense prediction. ArXiv preprint (2021) [7](#)
25. Ranftl, R., Lasinger, K., Hafner, D., Schindler, K., Koltun, V.: Towards robust monocular depth estimation: Mixing datasets for zero-shot cross-dataset transfer. IEEE Transactions on Pattern Analysis and Machine Intelligence (TPAMI) (2020) [7](#)
26. Rombach, R., Blattmann, A., Lorenz, D., Esser, P., Ommer, B.: High-resolution image synthesis with latent diffusion models. In: Proceedings of the IEEE/CVF conference on computer vision and pattern recognition. pp. 10684–10695 (2022) [7](#)
27. Schönberger, J.L., Frahm, J.M.: Structure-from-motion revisited. In: Conference on Computer Vision and Pattern Recognition (CVPR) (2016) [4](#)
28. Schönberger, J.L., Zheng, E., Pollefeys, M., Frahm, J.M.: Pixelwise view selection for unstructured multi-view stereo. In: European Conference on Computer Vision (ECCV) (2016) [4](#)
29. Somraj, N., Soundararajan, R.: Vip-nerf: Visibility prior for sparse input neural radiance fields (August 2023). <https://doi.org/10.1145/3588432.3591539> [4](#), [19](#)
30. Srinivasan, P.P., Tucker, R., Barron, J.T., Ramamoorthi, R., Ng, R., Snavely, N.: Pushing the boundaries of view extrapolation with multiplane images. CVPR (2019) [4](#)

31. Stan, G.B.M., Wofk, D., Fox, S., Redden, A., Saxton, W., Yu, J., Aflalo, E., Tseng, S.Y., Nonato, F., Muller, M., et al.: Ldm3d: Latent diffusion model for 3d. arXiv preprint arXiv:2305.10853 (2023) [7](#)
32. Sun, X., Wu, J., Zhang, X., Zhang, Z., Zhang, C., Xue, T., Tenenbaum, J.B., Freeman, W.T.: Pix3d: Dataset and methods for single-image 3d shape modeling. In: IEEE Conference on Computer Vision and Pattern Recognition (CVPR) (2018) [8](#)
33. Tancik, M., Srinivasan, P., Mildenhall, B., Fridovich-Keil, S., Raghavan, N., Singhal, U., Ramamoorthi, R., Barron, J., Ng, R.: Fourier features let networks learn high frequency functions in low dimensional domains. *Advances in Neural Information Processing Systems* **33**, 7537–7547 (2020) [12](#)
34. Tang, J., Ren, J., Zhou, H., Liu, Z., Zeng, G.: Dreamgaussian: Generative gaussian splatting for efficient 3d content creation. arXiv preprint arXiv:2309.16653 (2023) [3](#), [7](#)
35. Tucker, R., Snavely, N.: Single-view view synthesis with multiplane images. In: Proceedings of the IEEE/CVF Conference on Computer Vision and Pattern Recognition. pp. 551–560 (2020) [4](#)
36. Wang, G., Chen, Z., Loy, C.C., Liu, Z.: Sparsenerf: Distilling depth ranking for few-shot novel view synthesis. *IEEE/CVF International Conference on Computer Vision (ICCV)* (2023) [4](#), [7](#), [11](#)
37. Wang, Z., Bovik, A., Sheikh, H., Simoncelli, E.: Image quality assessment: from error visibility to structural similarity. *IEEE Transactions on Image Processing* **13**(4), 600–612 (2004). <https://doi.org/10.1109/TIP.2003.819861> [12](#)
38. Weng, C.Y., Curless, B., Srinivasan, P.P., Barron, J.T., Kemelmacher-Shlizerman, I.: HumanNeRF: Free-viewpoint rendering of moving people from monocular video. In: Proceedings of the IEEE/CVF Conference on Computer Vision and Pattern Recognition (CVPR). pp. 16210–16220 (June 2022) [3](#)
39. Wu, G., Yi, T., Fang, J., Xie, L., Zhang, X., Wei, W., Liu, W., Tian, Q., Wang, X.: 4d gaussian splatting for real-time dynamic scene rendering. arXiv preprint arXiv:2310.08528 (2023) [3](#)
40. Xu, D., Jiang, Y., Wang, P., Fan, Z., Shi, H., Wang, Z.: Sinnerf: Training neural radiance fields on complex scenes from a single image (2022) [8](#)
41. Xu, D., Jiang, Y., Wang, P., Fan, Z., Wang, Y., Wang, Z.: Neurallift-360: Lifting an in-the-wild 2d photo to a 3d object with 360° views (2022) [7](#)
42. Yi, T., Fang, J., Wu, G., Xie, L., Zhang, X., Liu, W., Tian, Q., Wang, X.: Gaussiandreamer: Fast generation from text to 3d gaussian splatting with point cloud priors. arXiv preprint arXiv:2310.08529 (2023) [3](#)
43. Zhang, X., Srinivasan, P.P., Deng, B., Debevec, P., Freeman, W.T., Barron, J.T.: Nerfactor: Neural factorization of shape and reflectance under an unknown illumination. *ACM Transactions on Graphics (ToG)* **40**(6), 1–18 (2021) [3](#)
44. Zhou, T., Tucker, R., Flynn, J., Fyffe, G., Snavely, N.: Stereo magnification: Learning view synthesis using multiplane images. arXiv preprint arXiv:1805.09817 (2018) [4](#)
45. Zhu, Z., Fan, Z., Jiang, Y., Wang, Z.: Fsgs: Real-time few-shot view synthesis using gaussian splatting (2023) [4](#)
46. Zielonka, W., Bagautdinov, T., Saito, S., Zollhöfer, M., Thies, J., Romero, J.: Drivable 3d gaussian avatars. arXiv preprint arXiv:2311.08581 (2023) [3](#)
47. Zwicker, M., Pfister, H., van Baar, J., Gross, M.: Ewa volume splatting. In: Proceedings Visualization, 2001. VIS '01. pp. 29–538 (2001). <https://doi.org/10.1109/VISUAL.2001.964490> [3](#)

48. Zwicker, M., Pfister, H., Van Baar, J., Gross, M.: Surface splatting. In: Proceedings of the 28th annual conference on Computer graphics and interactive techniques. pp. 371–378 (2001) [3](#)

## Supplementary Contents

This supplementary is organized as follows:

- Sec. [F](#) shows the **gradient derivation** for our softmax depth formulation.
- Sec. [G](#) provides additional **quantitative and qualitative** comparisons on the Mip-NeRF 360 dataset.
- Sec. [H](#) provides additional ablation studies on the SDS loss, number of training views, and softmax depth formulation.

## F Derivation of the Softmax Depth Gradient

In this section, we derive the gradients used for the softmax depth implemented in the rasterizer. We assume we are rendering a single pixel and that the gaussians  $G_i$  along the camera ray are ordered from closest to the camera plane to the farthest. (i.e.  $\alpha_1$  corresponds to the gaussian closest to the camera, while  $\alpha_N$  corresponds to the farthest)

If we let  $w_k = T_k \alpha_k$  and  $T_k = \prod_{i=1}^{k-1} (1 - \alpha_i)$

$$d_{x,y}^{\text{softmax}} = \log \left( \frac{\sum_{i=1}^N w_i e^{\beta w_i} d_i}{\sum_{i=1}^N w_i e^{\beta w_i}} \right) \quad (14)$$

The derivative w.r.t the gaussian’s camera z value is given below:

$$\frac{\partial d_{x,y}^{\text{softmax}}}{\partial d_k} = \frac{w_k e^{\beta w_k}}{\sum_{i=1}^N w_i e^{\beta w_i} d_i} \quad (15)$$

The derivative w.r.t the gaussian’s alpha value is given below:

$$\frac{\partial d_{x,y}^{\text{softmax}}}{\partial \alpha_k} = \frac{(1 + \beta w_k) T_k e^{\beta w_k} d_k - \frac{1}{1 - \alpha_k} \sum_{j=k+1}^N (1 + \beta w_j) w_j e^{\beta w_j} d_j}{\sum_{i=1}^N w_i e^{\beta w_i} d_i} \quad (3)$$

$$- \frac{(1 + \beta w_k) T_k e^{\beta w_k} - \frac{1}{1 - \alpha_k} \sum_{j=k+1}^N (1 + \beta w_j) w_j e^{\beta w_j}}{\sum_{i=1}^N w_i e^{\beta w_i}} \quad (4)$$

The sums in the denominators are retained during the forward pass and subsequently transferred to the backward pass. To avoid an  $O(n^2)$  blowup, an accumulator strategy is used as in [\[11\]](#).

| Model        | PSNR $\uparrow$ | SSIM $\uparrow$ | LPIPS $\downarrow$ | Runtime (h) | Render FPS |
|--------------|-----------------|-----------------|--------------------|-------------|------------|
| SparseNeRF   | 11.5638         | 0.3206          | 0.6984             | 4           | 1/120      |
| Base 3DGS    | 15.3840         | 0.4415          | <u>0.5061</u>      | 0.5         | 120+       |
| Mip-NeRF 360 | <u>17.1044</u>  | <u>0.4660</u>   | 0.5750             | 3           | 1/120      |
| RegNeRF      | 11.7379         | 0.2266          | 0.6892             | 4           | 1/120      |
| ViP-NeRF     | 11.1622         | 0.2291          | 0.7132             | 4           | 1/120      |
| Ours         | <b>17.2558</b>  | <b>0.5067</b>   | <b>0.4738</b>      | 0.75        | 120+       |

**Table D: Additional sparse-view NeRF baselines.** Runtimes are recorded on 1 RTX3090. We out-perform all the tested baselines on PSNR, SSIM and LPIPS while also being significantly faster in both training and inferencing.

Let  $\mathcal{A}_k^l, \mathcal{A}_k^r$  be the accumulators pertaining to  $\frac{\partial d_{x,y}^{\text{softmax}}}{\partial \alpha_k}$  for expressions (3) and (4) respectively.

$$\begin{aligned}\mathcal{A}_0^l &= \mathcal{A}_0^r = 0 \\ \mathcal{A}_k^l &= \alpha_{k-1}(1 + \beta w_{k-1})e^{\beta w_{k-1}}d_{k-1} + (1 - \alpha_{k-1})\mathcal{A}_{k-1}^l \\ \mathcal{A}_k^r &= \alpha_{k-1}(1 + \beta w_{k-1})e^{\beta w_{k-1}} + (1 - \alpha_{k-1})\mathcal{A}_{k-1}^r\end{aligned}$$

It can be shown that

$$\frac{\partial d_{x,y}^{\text{softmax}}}{\partial \alpha_k} = T_k \left( \frac{(1 + \beta w_k)e^{\beta w_k}d_k - \mathcal{A}_k^l}{\sum_{i=1}^N w_i e^{\beta w_i}d_i} - \frac{(1 + \beta w_k)e^{\beta w_k} - \mathcal{A}_k^r}{\sum_{i=1}^N w_i e^{\beta w_i}} \right)$$

## G Additional Comparisons on Mip-NeRF 360 Dataset

In this section, we provide more extensive qualitative and quantitative comparisons on the Mip-NeRF 360 dataset. In Tab. D, we provide a more complete version of Table 1 from the main paper which includes rendering FPS and comparisons against ViP-NeRF [29], a NeRF-based technique for few-shot view synthesis. All models use 12 input images. Our model outperforms all prior models on PSNR, SSIM, and LPIPS and can render images at 120+ FPS, comparable to Base 3DGS and significantly faster than all NeRF based models.

In Fig. H and Fig. I, we provide additional qualitative results of both rendered images and depth maps. The images in Fig. H show that our models render images that are more consistent (fewer floaters and color artifacts) while also including high-frequency details. Fig. I compares depth maps rendered from base 3DGS models and our models. All depth maps are rendered using alpha-blending. Depth maps rendered from our model consistently include more detail and cover more range.

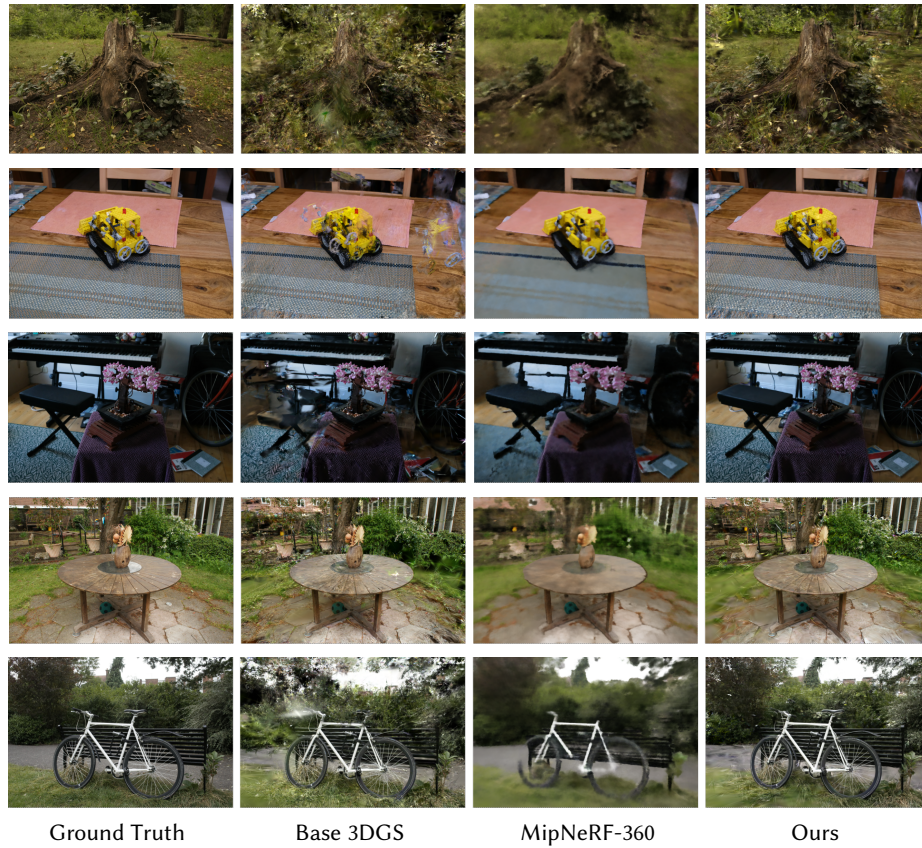


**Fig. H:** Qualitative Results on the MipNeRF-360 dataset. Scenes are 'Stump', 'Kitchen', 'Bonsai', 'Garden', and 'Bicycle'.

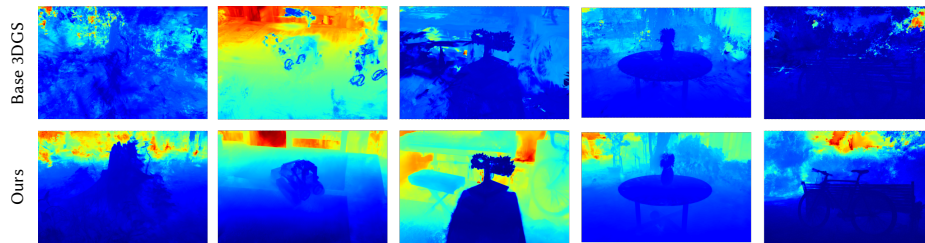


**Fig. I:** Depth renders from Base 3DGS (top) and our model (bottom) for 5 scenes from the MipNeRF-360 dataset: Stump, Kitchen, Bonsai, Garden, and Bicycle. Base 3DGS depths are generally incorrectly concentrated close to the camera view while our model learns more varied and detailed depths.

## H Additional Ablation Studies

In this section, we provide additional ablation studies on the effectiveness of the SDS loss, on the performance of our model as the number of training views changes, and the benefits of softmax depth.

**SDS Loss** Fig. J provides qualitative examples of models train with and without our SDS loss. While the models trained without the SDS loss generate reasonable images, they exhibit many high-frequency artifacts, likely the result of many small highly anisotropic gaussians. Models trained with the SDS loss are able to largely avoid this issue. This highlights the design of our SDS loss: we do not want the diffusion model to generate new details or unseen views, and instead want it to refine regions of our representation and alleviate some of the limitations of the 3D Gaussian representation.

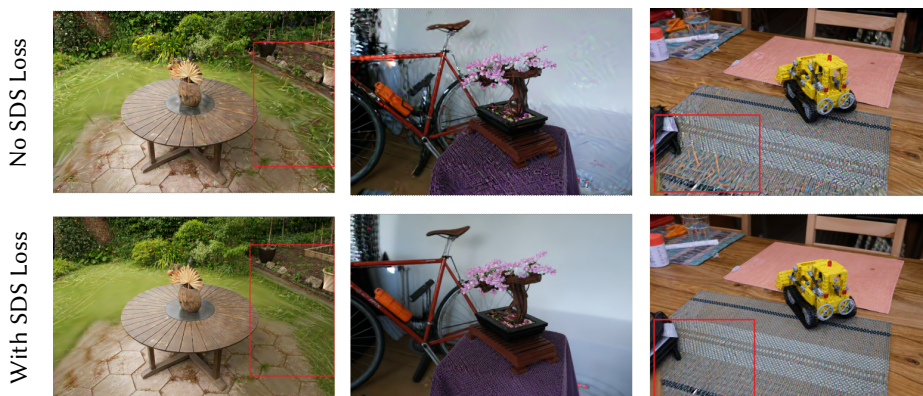


**Fig. J:** Qualitative ablation study on the benefits of the SDS loss. Images from models without the SDS loss (top) exhibit high-frequency artifacts and dis-coloration. Images from models with the SDS loss (bottom) smooth these artifacts out and have higher quality reconstructions.

**Number of Training Views** Fig. K provides a study of how our model performs relative to base 3DGS as the number of training views is changed. We test 8, 10, 12, 14, 16, and 18 views. Across all three metrics, PSNR, SSIM, and LPIPS, our model consistently outperforms Base 3DGS in all settings. Our models also perform well in the challenging 8-view setting, achieving results that are comparable to base 3DGS and better than most NeRF based methods at 12-view.

**Softmax Depth** In Tab. E we provide a quantitative comparison between alpha-blended depth and softmax depth for our depth correlation loss. We train 2

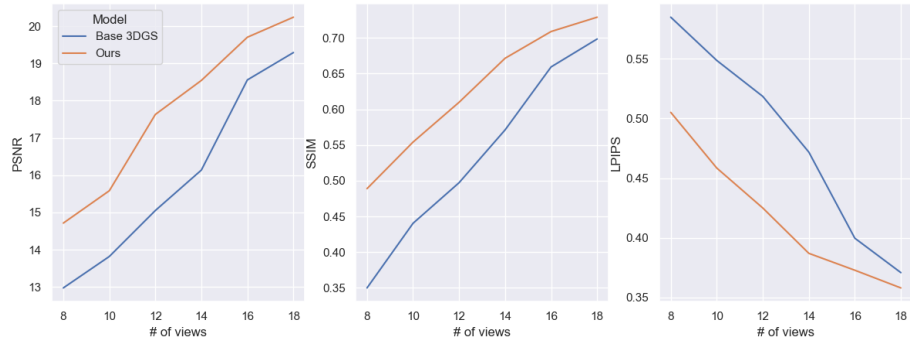


**Fig. K:** Ablation study on the number of views used to train models. Our models consistently outperform Base 3DGS on PSNR, SSIM, and LPIPS when we use as few as 8 or as many as 18 images for training.

models, both with only the depth correlation loss. One uses alpha-blended depth for this loss while the other uses softmax depth. On the full Mip-NeRF 360 dataset, the model trained with softmax depth correlation loss outperformed both base 3DGS and alpha-blended depth correlation loss, suggesting softmax depth can help the model learn better representations.

| Model                      | PSNR $\uparrow$ | SSIM $\uparrow$ | LPIPS $\downarrow$ |
|----------------------------|-----------------|-----------------|--------------------|
| Base 3DGS                  | 15.3840         | 0.4415          | 0.5061             |
| Base + Alpha-Blended Depth | 15.6749         | 0.4557          | 0.4998             |
| Base + Softmax Depth       | <b>16.5051</b>  | <b>0.4972</b>   | <b>0.4744</b>      |

**Table E:** Ablation study on the relative effectiveness of softmax depth vs alpha-blended depth.